An Investigation of Relative CEP Cycling in Birefringent Delay Lines

Mårten Carlsson

Thesis submitted for the degree of Bachelor of Science

Project duration: 2 months

Seminar date: 4 June, 2026

Supervised by Cord Arnold and Daniel Díaz Rivas

LRAP627(2026)

LUND UNIVERSITY

Division of Atomic Physics

Department of Physics

Abstract

Ultrafast pump-probe laser experiments often require precise control of both the temporal delay and electric field between pulses. Birefringent delay lines offer a compact alternative to traditional mirror-based systems, but introducing a group delay through material dispersion inherently causes the Carrier-Envelope Phase (CEP) to cycle differently in the pulses. This Relative CEP Cycling (RCC) prevents control of the electric field, limiting applications in few-cycle laser pulse experiments. This work demonstrates that by pairing the birefringent materials MgF_2 and sapphire, this cycling can be eliminated at a specific central wavelength. Through analytical calculations, computer simulations using Fourier Transform Spectral Interferometry (FTSI), and experimental characterization, a zero-cycling-rate central wavelength (λ_{ZCR}) is identified. This wavelength is where the Relative CEP Cycling Rate (RCCR) remains zero regardless of relative group delay. The experimentally measured ($\lambda_{ZCR} = 778.38 \pm 0.78$ nm) deviates from the analytically predicted value (749.59 nm) and the simulated value (747.11 ± 0.62 nm), partly due to variations in reported Sellmeier coefficients for these materials. Despite the identified discrepancy between values of λ_{ZCR}, the fundamental principle is validated: careful material selection enables birefringent delay lines that have precise control over the electric field, opening pathways for compact, robust few-cycle pulse control.

CONTENTS

List of Abbreviations

CEP	Carrier-Envelope Phase
RCC	Relative CEP Cycling
RCCR	Relative CEP Cycling Rate
GD	Group Delay
GDD	Group Delay Dispersion
TOD	Third Order Dispersion
ZCR	Zero-Cycling-Rate
FTSI	Fourier Transform Spectral Interferometry
FT	Fourier Transform
DC	Direct Current
MgF_2	Magnesium Fluoride
o	Ordinary axis
e	Extraordinary axis

1 Introduction

Ultrashort laser pulses are electromagnetic waves that span a very short duration, ranging from the femtosecond scale down to attoseconds. This short timescale makes it possible to probe the fundamental constituents of matter. The significance of this field was recently highlighted by the 2023 Nobel Prize in Physics, awarded to Anne L'Huillier and colleagues for their pioneering research in attosecond physics at Lund University [1]. Ultrashort laser pulses consist of a carrier field with an intensity envelope. For pulses in the few-cycle regime, i.e. when the envelope only stretches a few oscillations of the carrier, the alignment of the carrier field with the peak of the envelope, the so-called carrier-envelope phase (CEP), becomes important for light-matter interaction. When pulses propagate through dispersive media, the CEP shifts due to the difference between phase and group velocities.

Many practical applications of these ultrashort laser pulses require that two or more pulses are delayed with respect to each other. In traditional setups, delays are introduced by a difference in propagation distance through air using translation stages and mirrors, a configuration that requires careful alignment, occupies significant optical table space, and offers no intrinsic dispersion compensation. Birefringent delay lines offer an elegant alternative: a single, translating device made from two wedges of distinct materials (with at least one being birefringent) simultaneously splits the pulse into orthogonal polarizations and delays them by material dispersion. When light pulses propagate through the device, the ordinary and extraordinary polarizations experience different phase and group velocities, which results in a relative group delay between polarizations. This relative delay depends on the translation position of the device, allowing for precise tuning of the relative group delay. This concept was first introduced by Brida et al. in 2012 [2]. However, unlike propagation in air, the act of introducing a group delay difference between two pulses with a birefringent device inherently introduces a difference in how to CEP evolves, a phenomenon referred to as "relative CEP cycling" (RCC) in this work. For applications that require control over the electric field, this RCC is a major obstacle.

This work aims to investigate whether this type of delay system utilizing a combination of birefringent materials can generate two relatively delayed pulses while minimizing RCC. The aim of the project is highlighted in Figure 1. To achieve this, a combination of methodologies is used. Firstly, analytical calculations and computer simulations are performed to investigate how the birefringent device affects the propagating light. The computer simulations rely on Sellmeier coefficients for the refractive index to extract the simulated phase accumulations. To analyze interference spectra from laser pulses delayed by these systems, a Fourier Transform Spectral Interferometry (FTSI) method is employed [3]. Secondly, experimental characterization of the delay line is performed in the lab and subsequently analyzed with the same methodology as in the computer simulations.

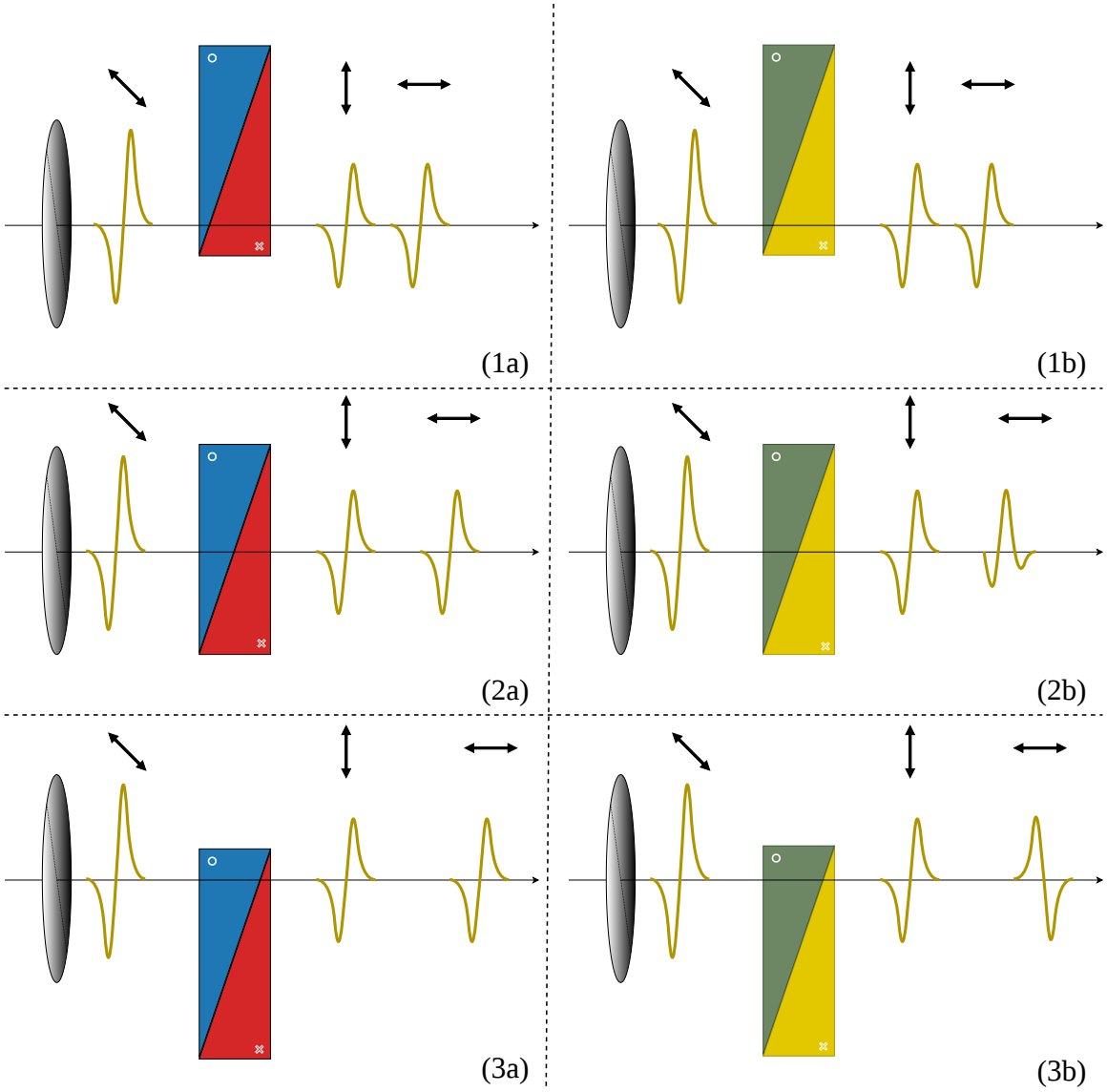

Figure 1: Six illustrative schematics demonstrating how different material combinations in a birefringent delay device affect outgoing cross-polarized pulses at various translation positions. Each row corresponds to a specific translation position (varying the propagation distance of each material), while each column represents a different material combination. Black arrows indicate the polarization of the pulses as seen along the optical axis. The goal of the project is to identify a material combination that yields the behavior shown in the left column: the outgoing pulses maintain a relative Carrier-Envelope Phase (CEP) regardless of the relative group delay introduced. This is in stark contrast to the right column, where the relative CEP of the outgoing pulses is altered depending on the translation position.

2 Background

This chapter establishes the theoretical foundation required to understand the generation and control of delayed ultrashort pulses. Firstly, a mathematical definition of the electric field of an ultrashort pulse is presented. Next, a laser pulse's propagation through dispersive media is explored, ultimately combining these concepts to detail the principles of using a birefringent delay line for interferometry. The theoretical concepts and derivations presented throughout this section are primarily based on [4].

2.1 Ultrashort laser pulses

An ultrashort laser pulse consists of two elements: an underlying continuous sinusoidal wave called the carrier field, and an envelope. The envelope shapes the carrier to form a finite pulse, typically modeled with a Gaussian shape in the time domain. Neglecting polarization and spatial dependence, the electric field of a laser pulse can be expressed mathematically as:

$$E(t) = A_0(t) \exp(i\omega_0 t), \tag{1}$$

where A_0 is the complex envelope and ω_0 is the carrier angular frequency.

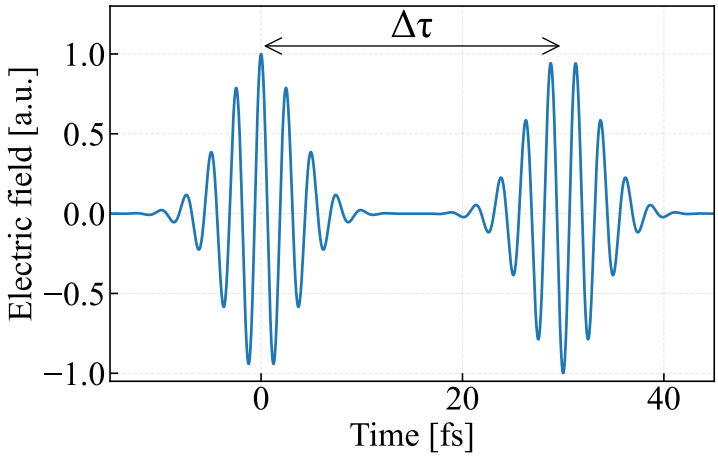

Figure 2: Simulated total electric field of two 12 fs pulses in the time domain. The pulses are separated by an artificial relative time delay of $\Delta\tau = 30$ fs and the rightmost pulse's carrier is shifted by $\Delta\phi_0 = \pi$ relative to the left pulse. The central wavelength is $\lambda_0 = 750$ nm for the carrier wave.

The whole pulse can be shifted in time by replacing the variable t with $(t - \Delta\tau)$, and the carrier can be shifted by adding a phase term, $\Delta\phi_0$. Examining the superposition of two pulses, where one is shifted relative to the other in this way, yields the following result:

$$E_{\text{tot}}(t) = E_1(t) + E_2(t - \Delta\tau)e^{i\Delta\phi_0}. \tag{2}$$

Equation 2 is visually represented in Figure 2.

If two pulses are displaced in time they form fringes in the spectral domain. These interference fringes can be observed in the spectral domain by applying the Fourier transform to Equation 2. The characteristics of these fringes are dependent on the placement of the electric field inside the envelope, allowing for $\Delta\phi_0$ and $\Delta\tau$ to be extracted from them. Assuming identical spectral amplitudes for both pulses, the interference in the spectral domain is expressed as:

$$\tilde{E}(\omega) = \int_{-\infty}^{\infty} E_{\text{tot}}(t)e^{-i\omega t}dt \quad \Rightarrow \quad \tilde{E}(\omega) = \tilde{A}_0(\omega)\left[1 + e^{i(\Delta\phi_0 - \omega\Delta\tau)}\right], \tag{3}$$

where ω is the angular frequency of the light. The experimentally observable quantity is the spectral intensity, which has the form

$$I(\omega) = |\tilde{E}(\omega)|^2 \quad \Rightarrow \quad I(\omega) = 2I_0(\omega)\left[1 + \cos(\Delta\phi_0 - \omega\Delta\tau)\right]. \tag{4}$$

This behavior is illustrated in Figure 3. The fringes presented here are, more formally, denoted as spectral interferograms.

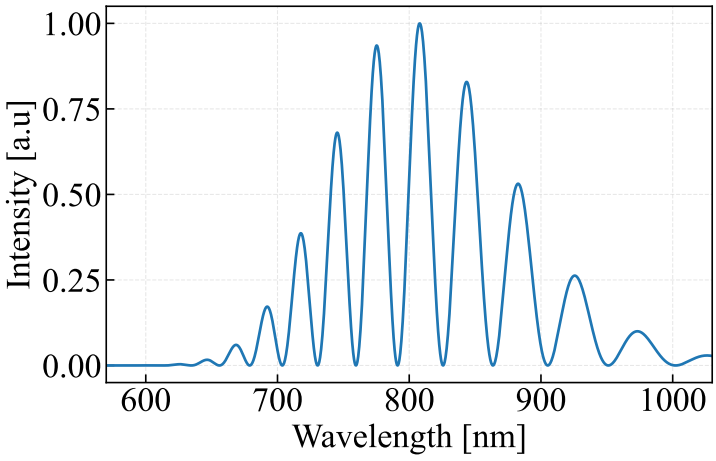

Figure 3: Spectral interferogram simulated from 12 fs transform-limited Gaussian pulses separated by $\Delta\tau = 63$ fs, demonstrating the behavior found in Equation 4. The asymmetry seen in fringe periodicity primarily arises from the horizontal axis being converted to wavelength.

2.1.1 Carrier-envelope phase

The carrier-envelope phase (CEP) is defined as the phase difference between the underlying oscillating carrier wave and the peak of the envelope. The speed of the carrier's

propagation is denoted as phase velocity, v_p, and the speed of the envelope is denoted as group velocity, v_g. When these speeds do not match, the relative phase between the carrier and the envelope shifts. Four different values of the carrier-envelope phase are presented in Figure 4.

Building upon the two-pulse interference described in the previous section, the relative CEP cycling between two pulses with a group delay difference can be extracted from the spectral fringes. Specifically, the argument of the interference term evaluated at the central frequency, ω_0, yields the relative CEP cycling, which can be expressed as:

$$\Delta\text{CEP} = \Delta\phi_0 - \omega_0\Delta\tau. \tag{5}$$

Equation 5 dictates that the relative CEP shift is the difference in carrier phase minus the difference in envelope phase. It is important to note that zero relative CEP cycling does not strictly mean that the carrier stays in the same position relative to the peak of the envelope in any of the pulses, rather that the CEP cycles at the same rate in the two pulses. This concept and the relationship shown in Equation 5 are both fundamental pieces of this thesis.

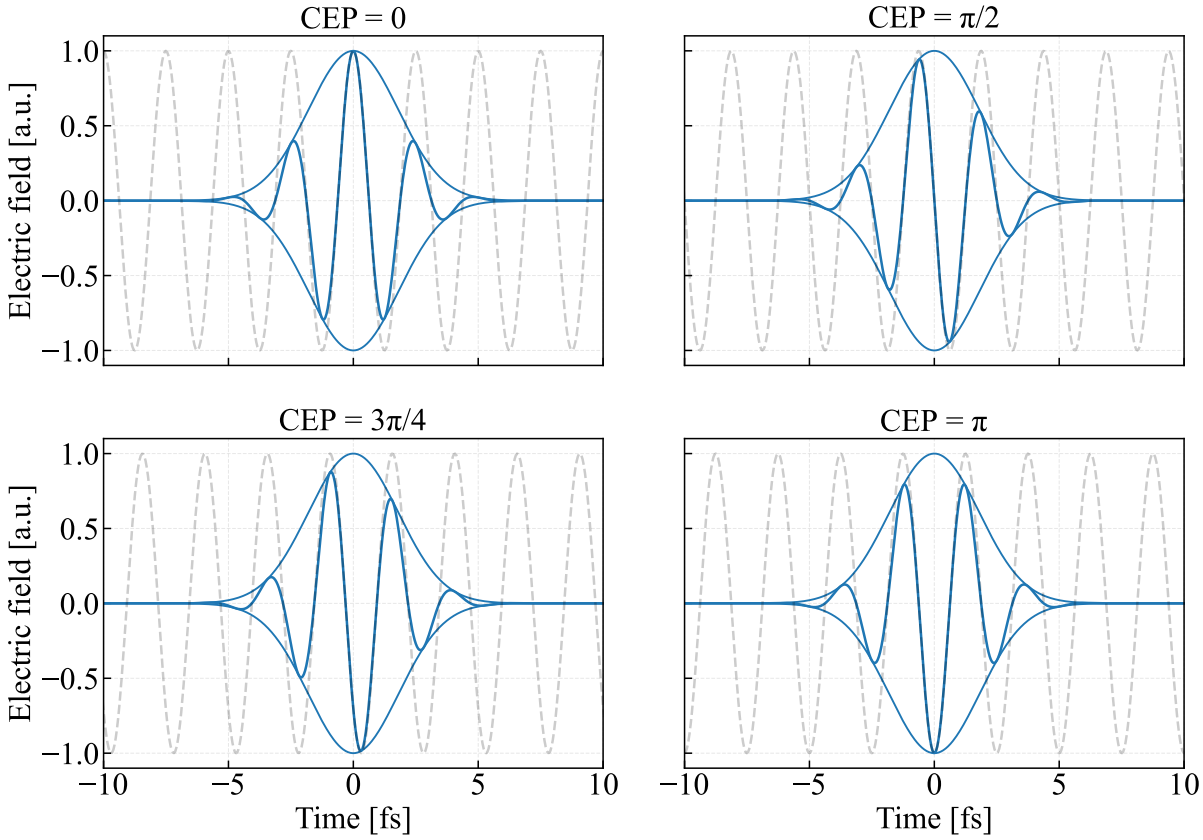

Figure 4: Temporal profiles of a 6 fs Gaussian laser pulse at four different carrier-envelope phase values, demonstrating the shift of the electric field relative to the envelope. The central wavelength is $\lambda_0 = 750$ nm for the carrier wave.

2.2 Refractive Index and Material Dispersion

When low-intensity light propagates through a solid dielectric medium, its oscillating electric field acts as a driving force on the material's bound electrons. Under the classical oscillator model, these electrons can be conceptually treated as point masses on springs. As they are driven by the incident light, they re-emit secondary electromagnetic waves. The macroscopic interference between the incident light and these secondary waves effectively delays the propagating wave, manifesting as a positive refractive index.

Because an electron's physical response depends on how close the driving frequency is to its natural resonance, this macroscopic delay is inherently frequency dependent. This phenomenon, known as material dispersion, dictates that the refractive index varies with wavelength, which is exactly what causes the phase and group velocities of an ultrashort pulse to differ. To accurately model this wavelength dependence across a broad spectrum, the refractive index is typically expressed using an empirical Sellmeier equation of the form:

$$\mathrm{n}(\lambda)^2 = 1 + \sum_i \frac{B_i \lambda^2}{\lambda^2 - C_i}, \tag{6}$$

where $\mathrm{n}(\lambda)$ is the refractive index, λ is the wavelength of the light, B_i and C_i are experimentally determined Sellmeier coefficients for a given material.

The Sellmeier equation is strictly valid only within specific wavelength ranges, though three or four terms are typically sufficient for accurate modeling. Using this function for the refractive index one can determine the phase that light accumulates through such a medium with:

$$\varphi(\omega) = \omega \frac{n(\omega) d}{c_0}, \tag{7}$$

where c_0 is the speed of light in vacuum and d is the distance the light propagates in the medium. This equation implies that the phase inherits the complexity of the refractive index, which shifts the light by different amounts depending on its frequency.

2.2.1 Phase expansion

To analyze how the phase affects ultrashort laser pulses, one can use Taylor expansion. Taylor expansion of the phase centered at a central angular frequency, ω_0, yields physically meaningful coefficients.

$$\phi(\omega) = \phi(\omega_0) + \underbrace{\phi'(\omega_0)}_{\mathrm{GD}} \cdot (\omega - \omega_0) + \frac{1}{2!} \underbrace{\phi''(\omega_0)}_{\mathrm{GDD}} \cdot (\omega - \omega_0)^2 + \ ... \tag{8}$$

The expansion terms give insight into how the pulse is affected. The first term is the absolute phase and corresponds to a phase-shift for the central frequency. The second term represents the group delay (GD), which quantifies the temporal delay imposed on the envelope. This corresponds to the overall time shift of the pulse after propagation. In this work, the difference in group delay between the two pulses (evaluated at the central frequency) is used interchangeably with $\Delta\tau$. The third term, Group Delay Dispersion (GDD), is the primary term dominating the contribution to temporal broadening of the pulses. For the sake of simplicity, and due to their typically small contribution, higher order terms are neglected in this work. All pulses are affected by these phase effects, but due to the time-frequency Fourier relationship, a temporally short pulse inherently exhibits a broader spectral bandwidth. Because it possesses this broader bandwidth, a shorter pulse interacts with a wider range of the frequency-dependent phase, making the complex dispersion dynamics much more pronounced compared to narrowband, longer-duration pulses.

While higher-order terms like GDD and Third Order Dispersion (TOD) profoundly distort and broaden the pulse envelope (as seen in Figure 6), they do not independently shift the position of the underlying carrier wave at the central frequency. As shown by its definition in Equation 5, the relative shift between the carrier and the envelope is strictly governed by the absolute phase, $\Delta\phi(\omega_0)$, and the difference in group delay, $\Delta\phi'(\omega_0)$ (also denoted ΔGD or $\Delta\tau$). This allows for precise extraction of the relative CEP cycling without being conflated by the phase effects caused by higher order dispersion terms.

2.2.2 Birefringence

Birefringence is a property wherein a material possesses two principal axes with distinct refractive indices: the ordinary axis and extraordinary axis. This gives such a medium different dispersive properties along each of the axes. If the axes are aligned to the polarization of two cross-polarized pulses, each of the pulses is affected by two completely different refractive indices while propagating in the same material. The refractive indices of both axes for the relevant materials in this project are plotted in Figure 5.

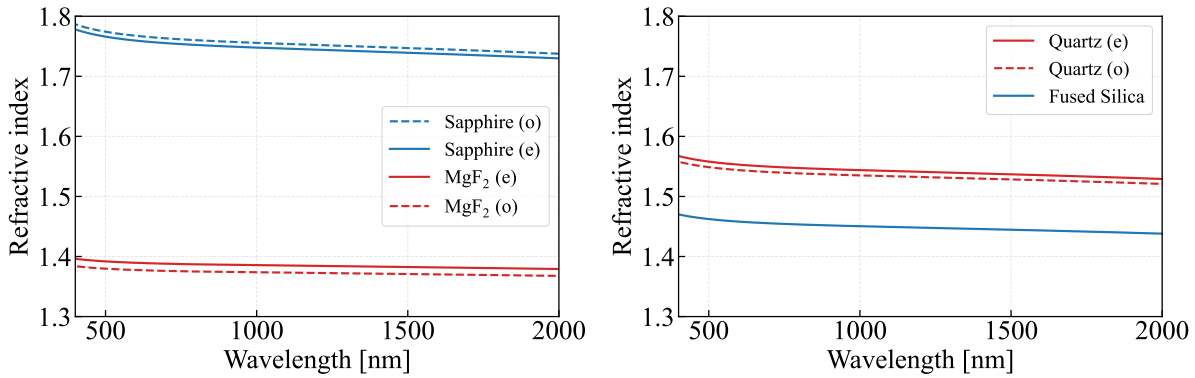

Figure 5: Refractive indices (extraordinary and ordinary) as a function of wavelength for the materials: MgF_2/sapphire (left) and quartz/fused silica (right) [5, 6, 7, 8].

The fact that two cross-polarized pulses are affected differently in a birefringent medium is highlighted in Figure 6.

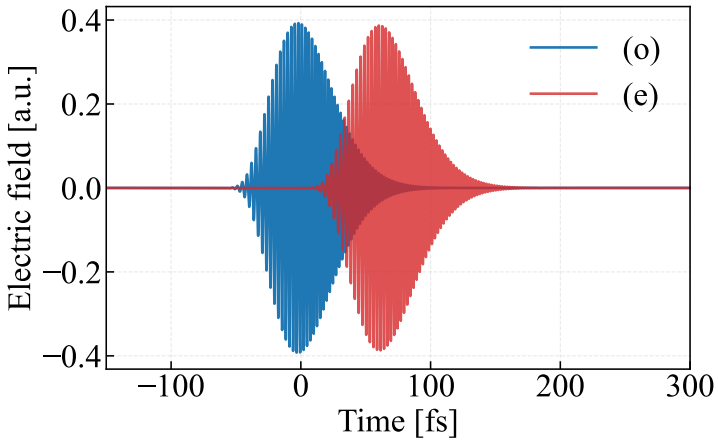

Figure 6: Simulated temporal profiles of two cross-polarized, 12 fs transform-limited Gaussian pulses (left pulse in Figure 2) after propagating through 2 mm of quartz. The blue and red lines correspond to polarizations along the ordinary and extraordinary axes, respectively. The time axis is shifted to be centered on the ordinary-axis pulse for visual comparison. The pulses exhibit delay, broadening, and asymmetry governed by the material's group delay (GD), group delay dispersion (GDD), and third-order dispersion (TOD). The relative differences between the two pulses are $\Delta GD \approx 63$ fs, $\Delta GDD \approx 2.6$ fs^2, and $\Delta TOD \approx 2.4$ fs^3

2.3 Birefringent delay line

Birefringent delay systems were first introduced in 2012 by D. Brida et al. [2]. Its simplest form is a single delay device that consists of two wedges made of two distinct materials, as seen in Figure 7. This device is placed on a translation stage that moves the device orthogonally to the optical axis; this movement is referred to as translation. This makes the propagation distance through each material highly tunable. The purpose of this system is to achieve greater control of the spectral phase difference between pulses.

An interferometer can be constructed using the delay device placed between two polarizers. Polarizer 1 projects the incident laser pulse into a 45 degree, linear polarization relative to the orientation of the device's birefringent axes. The resulting polarization has equal amplitude in both principal axes of the birefringent materials. Because these two orthogonal components travel at different group velocities due to the material's birefringence, the incident light's two polarization components are effectively split into two independent, cross-polarized pulses. After propagating through the device, Polarizer 2 has the function of recombining these cross-polarized pulses, summing their spectral contributions to form the final interferogram.

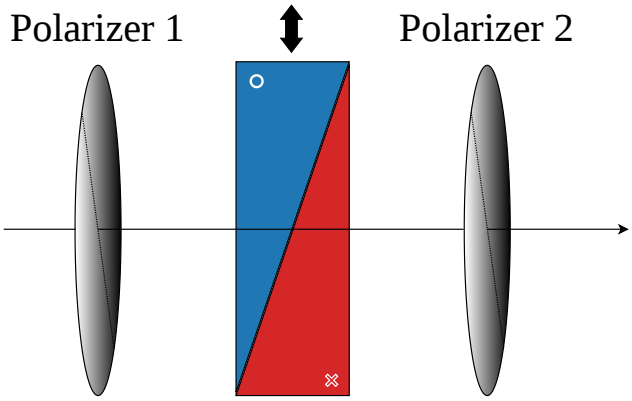

Figure 7: A schematic of the active components of the birefringent delay line utilized as an interferometer. Polarizer 1 and 2 are set to a relative degree of 0 or 180 degrees. Arrow indicating the translation stage direction of the wedge. 'O' and 'X' indicating that the materials are combined orthogonally with respect to one of their birefringent axes.

During translation, a phase difference accumulates because the two materials have distinct refractive indices. This phase difference is utilized to delay the pulses. This allows the system to act as a precisely controllable cross-polarized, two-pulse delay line. A difference in delay between the pulses, by definition, means a difference in first order derivative of the phase accumulation between the A and B axes. According to Equation 5, this implies that relative CEP cycling occurs unless the difference in absolute phase exactly compensates for the phase-shift of the envelope introduced by the group delay difference. To achieve this, the wedges are made of two distinct birefringent materials, MgF_2/sapphire and quartz/fused silica are the two material combinations used here. In this project, their birefringent axes are oriented orthogonally to one another. Consequently, the two cross-polarized pulses experience an inverted sequence of refractive indices. More precisely, the A-polarized pulse is polarized along the extraordinary (e) axis of the first material and the ordinary (o) axis of the second material. Conversely, the B-polarized pulse is polarized along the ordinary (o) axis of the first material and the extraordinary (e) axis of the second.

To mathematically formalize this compensation mechanism, the relationship found in Equation 5 can be expanded in terms of the refractive index. This then yields that the CEP cycling in one birefringent material can be expressed as:

$$\Delta\text{CEP} = \frac{\omega_0 z}{c_0}\Delta\text{n}(\omega_0) - \frac{\omega_0 z}{c_0}\Delta\left(\frac{d}{d\omega}(\text{n}(\omega)\omega)\right)\Bigg|_{\omega_0}, \tag{9}$$

where $\Delta\text{n}(\omega) = n_e(\omega) - n_o(\omega)$ is the birefringence of the material.

By applying the product rule to the derivative term, the absolute phase components exactly cancel each other. This simplifies the expression elegantly, demonstrating that the CEP cycling depends strictly on the instantaneous slope of the material's birefringence:

$$\Delta\text{CEP} = -\frac{\omega_0^2 z}{c_0}\Delta\frac{d\text{n}(\omega)}{d\omega}\Bigg|_{\omega_0}. \tag{10}$$

When extending this principle to the delay line consisting of two sequential materials with effective propagation distances z_1 and z_2, the total relative CEP cycling becomes:

$$\Delta\text{CEP}_{\text{RCC, total}} = -\frac{\omega_0^2}{c_0}\left(z_1\Delta\frac{d\text{n}_1(\omega)}{d\omega}\Bigg|_{\omega_0} \pm\ z_2\Delta\frac{d\text{n}_2(\omega)}{d\omega}\Bigg|_{\omega_0}\right). \tag{11}$$

If the condition in the equation above equals zero, it means that no matter where the wedge is under translation, the CEP evolves in the same way in both the A and B polarized pulses. The central hypothesis of this work is that the MgF_2/sapphire material combination may fulfill this condition (as opposed to quartz/fused silica) at a specific wavelength, which is investigated through simulation and experiment.

The $\pm$ sign is dictated by whether the birefringent axes of the two materials are aligned or crossed. To design a delay line where the relative CEP cycling rate is strictly zero during wedge translation, the net contribution of the terms inside the parenthesis must perfectly balance. However, in this work the two wedges are the same dimensions, which means only the material properties (and not propagation distance) are balanced in the birefringent delay line. In other words, a central wavelength where the instantaneous slope of the first material perfectly mirrors that of the second material is sought after. The relationship from Equation 11 is visualized in Figure 8 for quartz/fused silica (fused silica does not contribute since it is isotropic) and MgF_2/sapphire.

Because these phase additions are inherently wavelength-dependent, this perfect cancellation is not universal. However, by carefully selecting the material combination, this condition can be satisfied for a specific central wavelength. At this specific wavelength, denoted as the zero-cycling-rate wavelength (λ_{ZCR}), the difference in CEP cycling be-

tween the two pulses remains constant throughout the entire translation of the wedge, completely eliminating relative CEP cycling.

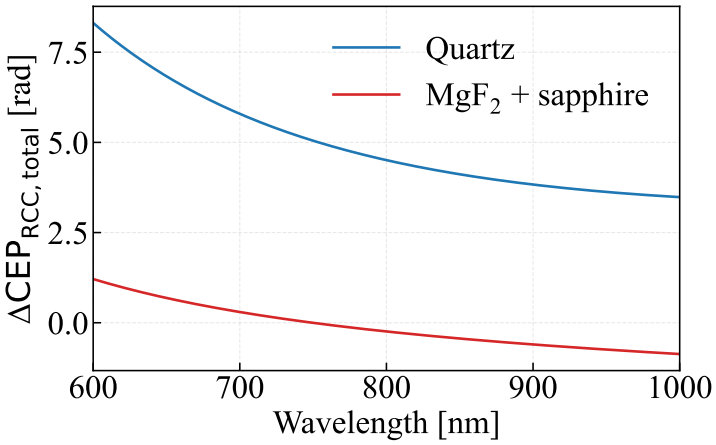

Figure 8: The expression for $\Delta\text{CEP}_{\text{RCC, total}}$ found in Equation 11 plotted over wavelength. The values for propagation distances are $z_1 = z_2 = 1$ mm. A zero-crossing in these curves indicates a central wavelength where the net contribution of the terms inside the parenthesis in Equation 11 perfectly balance. At this central wavelength, the relative CEP cycling is completely eliminated during wedge translation.

3 Simulation and Modeling

This chapter details the simulation framework developed to evaluate the difference in carrier-envelope phase cycling of a birefringent delay system. The methodology is divided into two primary steps: the theoretical generation of spectral interferograms, and the subsequent extraction of the Relative CEP Cycling (RCC) via Fourier Transform Spectral Interferometry (FTSI). Following the methodology, the simulated results are presented for the quartz/fused silica and MgF_2/sapphire material combinations.

3.1 Simulation methodology

To ensure the simulations accurately reflect laboratory conditions, the light is simulated with a lab-measured spectrum from the experimental light source. This spectrum provides a more realistic intensity envelope for the simulated pulses.

3.1.1 Refractive Index and Phase Modeling

To calculate phase for the simulations, the refractive index Sellmeier coefficients for all relevant materials are required. However, variations in published Sellmeier coefficients represent a significant source of uncertainty to account for when analyzing the results. To illustrate this, Figure 9 shows the discrepancy found in refractive index for MgF_2 between different sources. For this work, the specific coefficients are selected based on

their appropriate temperature conditions, relevant spectral ranges, and the recency of the data. For all subsequent simulations, the coefficients reported by Zheng et al. (2023) are chosen for MgF_2 [5], Dodge (1986) for sapphire [6], Ghosh (1999) for quartz [7], and Malitson (1965) for fused silica [8]. Importantly, while these literature variations affect the exact numerical relative CEP cycling, they do not alter the fundamental physical principles demonstrated in this study.

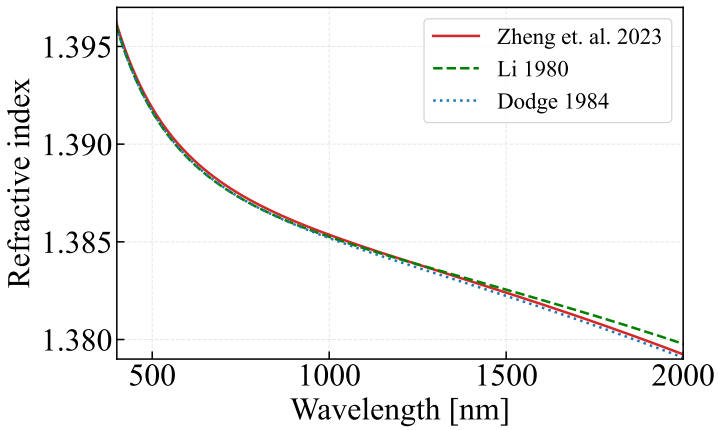

Figure 9: Refractive index curves of MgF_2 (extraordinary axis) as defined by the Sellmeier equations and coefficients found in Dodge 1984 [9], Zheng et al. 2023 [5], and H.H. Li 1980 [10].

With the refractive index of the relevant materials, the phase introduced by the materials is calculated using Equation 7. With the material's phase profiles, the subsequent spectral interferograms can be generated after modeling the birefringent delay line properties. To ensure a rigorous comparison between the simulations and the experimental characterization, the simulated interferograms must be treated as raw experimental data and subjected to the identical phase-extraction process.

3.1.2 Fourier Transform Spectral Interferometry

Initial attempts to extract the phase from the interferograms relied on direct numerical peak-finding in the spectral domain. However, this approach proved highly susceptible to resolution limits and spectral noise. Consequently, a more robust method, Fourier Transform Spectral Interferometry (FTSI) [3], is employed.

In subsection 2.1, Equation 4 provides an idealized model for two-pulse interference, assuming two identical, undistorted pulse envelopes and also neglecting higher order dispersion terms. However, the actual pulses exiting the device (E_1 and E_2) possess distinct, complex temporal shapes. To accommodate for this, the approach is generalized using FTSI. Expressing the total spectral intensity $S(\omega)$ using the complex fields of the two distinct pulses:

$$S(\omega) = |E_1(\omega)|^2 + |E_2(\omega)|^2 + E_1(\omega)^* E_2(\omega) + E_1(\omega) E_2(\omega)^*. \tag{12}$$

By grouping the first two terms as the direct current (DC) term, $S_{DC}(\omega)$, and defining the interference term $f(\omega) = E_1(\omega)^* E_2(\omega) = A_1^* A_2 \exp(i\Delta\phi)$ the interferogram simplifies to:

$$S(\omega) = S_{DC}(\omega) + f(\omega) + f^*(\omega). \tag{13}$$

Applying the inverse Fourier transform to go to the pseudo-time domain yields

$$\tilde{S}(t) = \tilde{S}_{DC}(t) + \tilde{f}(t) + \tilde{f}^*(-t). \tag{14}$$

The direct current (DC) peak ($\tilde{S}_{DC}(t)$) is centered at $t = 0$; it contains only the individual spectra of the pulses, not the phase difference between them. The second term represents the positive peak and is shifted to $t = +\Delta\text{GD}$. It contains the complex phase difference inside $f(\omega)$. The third term is the negative peak, which is shifted to $t = -\Delta\text{GD}$. It contains the complex conjugate of the phase difference. Assuming the group delay difference ΔGD is large enough, these three peaks do not overlap in the pseudo-time domain. The pseudo-time domain peaks are plotted in Figure 10.

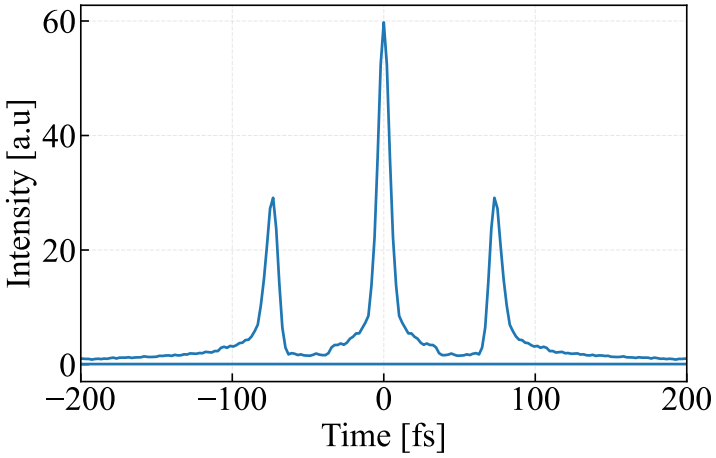

Figure 10: Pseudo-time domain showing three distinct peaks: negative peak at $-\Delta\text{GD}$ (left), DC peak at $t = 0$ (center), and positive peak at $+\Delta\text{GD}$ (right). The positive peak is extracted for analysis. The plot is produced by applying the inverse Fourier transform of a spectral interferogram at 73 fs relative group delay from a simulated quartz/fused silica delay line.

Because the phase information is entirely encoded in the cross-terms, only one of the side peaks is required. A Hann window [11] is applied in the pseudo-time domain to smoothly isolate the positive peak, effectively filtering out the DC and the redundant

negative conjugate peak. In the Fourier domain, a rectangular window corresponds to a sinc function. Simply multiplying by a boxcar in time means convolving with a sinc function in frequency, which creates artificial artifacts in the frequency domain known as the Gibbs phenomenon [12]. A smooth window, like the Hann window, tapers to zero gradually, suppressing the high-frequency artifacts. The effect of the Hann window on the positive peak is found in Figure 11.

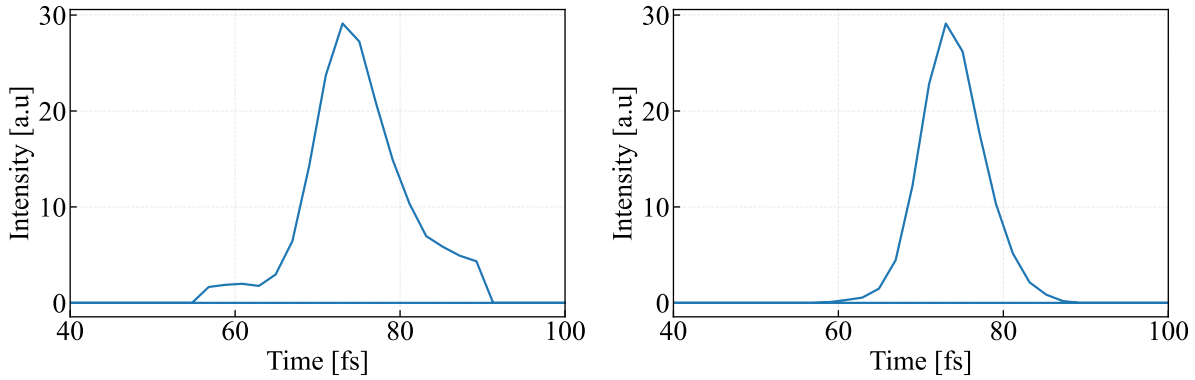

Figure 11: Left: the positive peak windowed by multiplying by a rectangular function. Right: the positive peak windowed using a Hann window.

With the smoothly windowed positive peak the Fourier transform is applied to go back into the spectral domain,

$$F\{f(t)\} = f(\omega) = A_1^* A_2 \exp(i\Delta\phi). \tag{15}$$

The total phase is extracted numerically from the argument of the complex exponent, yielding $\Delta\phi$. This is then fitted to a third order polynomial to find relevant coefficients, while not overfitting the data. Extracting the coefficients then reveals the difference in absolute phase and difference in group delay required to calculate the relative CEP cycling by Equation 5. The FTSI extraction is implemented in Python, with key code blocks provided in Appendix A.

3.2 Simulation results

This section is devoted to presenting the data acquired from the simulations of the two different material combinations: quartz / fused silica and MgF_2/sapphire. The focus lies in investigating whether or not MgF_2/sapphire significantly decreases the relative CEP cycling in a birefringent delay line. To benchmark the results, analytical calculations are performed. This analytical baseline is established by calculating the phase directly from the Sellmeier equations and applying a Taylor expansion to extract the difference in absolute phase ($\Delta\phi_0$) and difference in the group delay (ΔGD). With these two values, the RCC is calculated using Equation 5.

The translation movement of the device (shown in Figure 7) is simulated across its full range, and a spectral interferogram is recorded at each translation step. By stacking 1D intensity distributions of these spectral interferograms, their evolution can be visualized, producing what is known as spectrograms. The spectrograms for both material combinations utilized in the delay lines are presented in Figure 12. In these figures, the translation axis is converted to group delay difference for clearer physical interpretation.

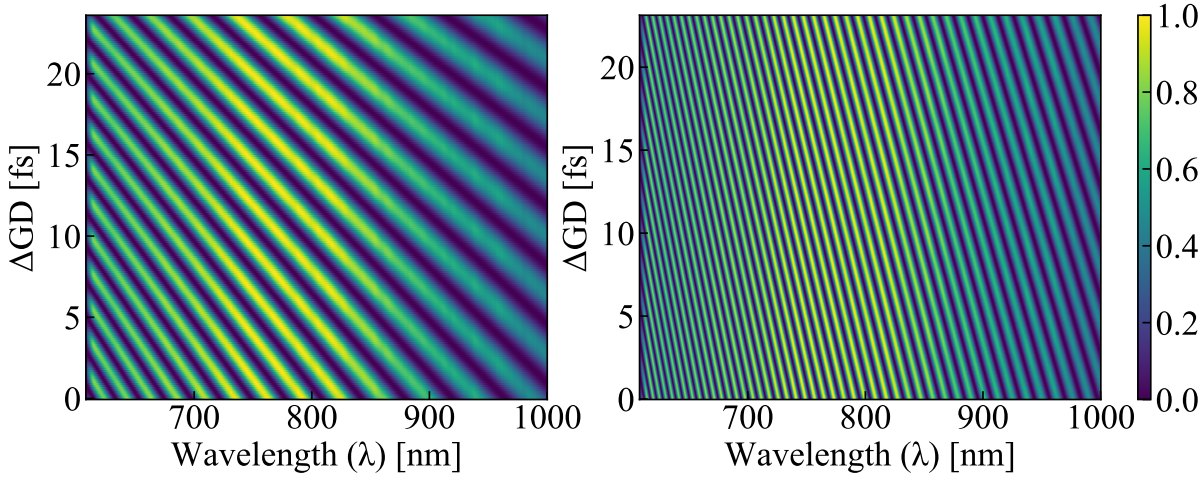

Figure 12: Quartz/fused silica (left). MgF_2/sapphire (right). Simulated spectrograms of the data simulated from both material combinations in the delay line. The spectral intensity is plotted over a 2D map of ΔGD and wavelength.

With this data, the FTSI methodology can be applied to find the relative CEP cycling. The RCC plotted over the difference in group delay is presented in Figure 13.

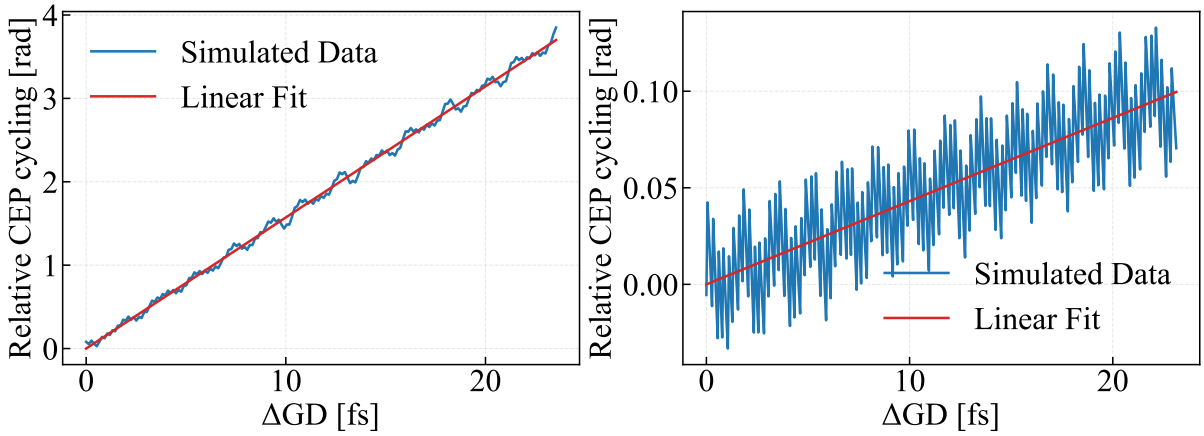

Figure 13: Quartz/fused silica (left). MgF_2/sapphire (right). The simulated relative CEP cycling plotted against ΔGD for both material combinations. The plots are generated using the FTSI method and a central wavelength of 750 nm. A linear function is fitted to the data.

A closer inspection of Figure 13 reveals an underlying sawtooth behavior beneath the

high-frequency noise. This periodicity, which is comparable to the period of the central wavelength of the laser, likely stems from residual spectral leakage of the DC or negative peaks into the isolated positive peak. Furthermore, the prominent noise observed in the simulated data is an artifact of the discrete time grid used in the numerical implementation. As the physical peak shifts continuously in time, the numerical windowing function only updates its position in discrete temporal bins. This sudden repositioning of the windowing function introduces artificial linear phase shifts, generating the observed oscillatory noise. While applying even further interpolation could mitigate these discretization errors, it would do so at the cost of increased computational complexity.

Nonetheless, while the extracted data exhibits this noise, the underlying trend remains clearly linear, justifying the use of linear regression to extract the Relative CEP Cycling Rate (RCCR). While this single-wavelength measurement quantifies the drift at the specific wavelength 750 nm, determining the system's more general behavior requires evaluating the RCCR across the entire operational spectrum. Therefore, the linear slope is extracted for a continuous range of central wavelengths to search for a potential zero-crossing. The RCCR over the operational spectrum is presented in Figure 14. The errors presented in the error bars and in the value of λ_{ZCR} is the standard fitting error from the third order polynomial fit of the FTSI-extracted phase.

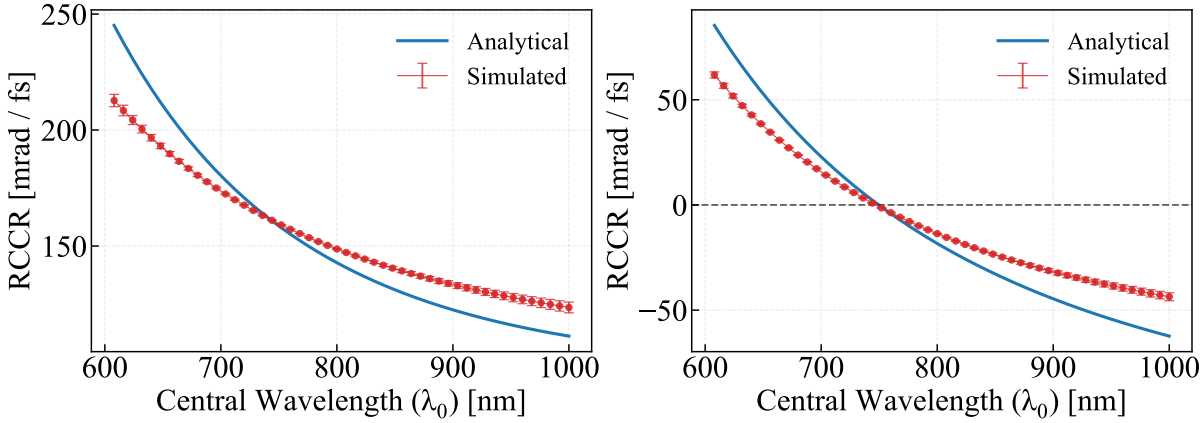

Figure 14: Left: the analytical (blue) and simulated (red) relative CEP cycling rate as a function of central wavelength of quartz/fused silica as calculated with FTSI. No λ_{ZCR} can be identified. Right: analytical and simulated curves for the MgF_2/sapphire material combination. Both curves cross a RCCR of 0 mrad/fs, with a λ_{ZCR} of 747.11 ± 0.62 nm in the simulation and 749.59 nm analytically.

As highlighted in Figure 14, the MgF_2/sapphire material combination successfully reaches a zero-cycling-rate in both the analytical and simulated curves. Conversely, the quartz/-fused silica material combination does not exhibit such a crossing and remains above 100 mrad/fs throughout the entire operational spectral range.

4 Experimental characterization

This section presents the experimental methods and data acquired from characterization of the two different material combinations: quartz / fused silica and MgF_2/sapphire. The primary objective is to experimentally verify whether the MgF_2/sapphire can function as birefringent delay lines with minimized relative CEP cycling.

4.1 Experimental methodology

The experimental setup, shown in Figure 15, utilizes a broadband super-continuum laser source. After passing through Polarizer 1, the light becomes linearly polarized at 45 degrees relative to the principal axis of the birefringent material. Following propagation through the birefringent delay line, a second polarizer, also oriented at 45 degrees, projects the cross-polarized pulses into the same polarization state to generate spectral interference. Although pictured in Figure 15, the delay compensation plate (1.8 mm of quartz) is excluded from the final measurements.

To ensure precise alignment through this system, a beam walking technique [13] is used. This is performed with two spatial reference points along the desired beam path in conjunction with two mirrors; “mirror 1” and “mirror 2”. To decouple the alignment process, the first reference point is aligned by adjusting only mirror 1 and the second reference point only with mirror 2. This ensures that the alignment converges as the process iterates.

Following recombination, an integrating sphere, consisting of a white diffusing box coupled into a fiber, captures the light and transmits it to a spectrometer. By spatially homogenizing the beam, the integrating sphere ensures that the spectrometer captures a true average of the spectral intensity, rendering the measurement robust against spatial variations in the beam profile and minimizing coupling errors at the fiber interface. A schematic of the physical setup is presented in Figure 15.

To compensate for the wavelength-dependent efficiency of the spectrometer, its known response function is applied to calibrate the recorded data. Once the final spectral interferograms are recorded, phase extraction is performed using the FTSI methodology detailed in subsubsection 3.1.2. The relative phase is mathematically extracted by calculating the complex argument of the isolated interference peak following the inverse Fourier transform.

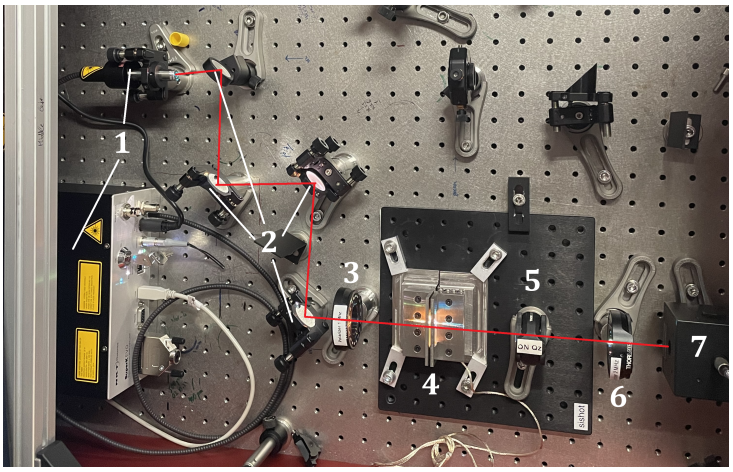

Figure 15: Laboratory optical setup. From left to right: the super-continuum source (1), a set of four mirrors to redirect the beam (2), Polarizer 1 (3), birefringent delay device (4), delay compensation plate (5), Polarizer 2 (6), and integrating sphere (7).

4.2 Experimental results

The experimental spectrograms retrieved from the quartz/fused silica and MgF_2/sapphire delay lines are presented in Figure 16.

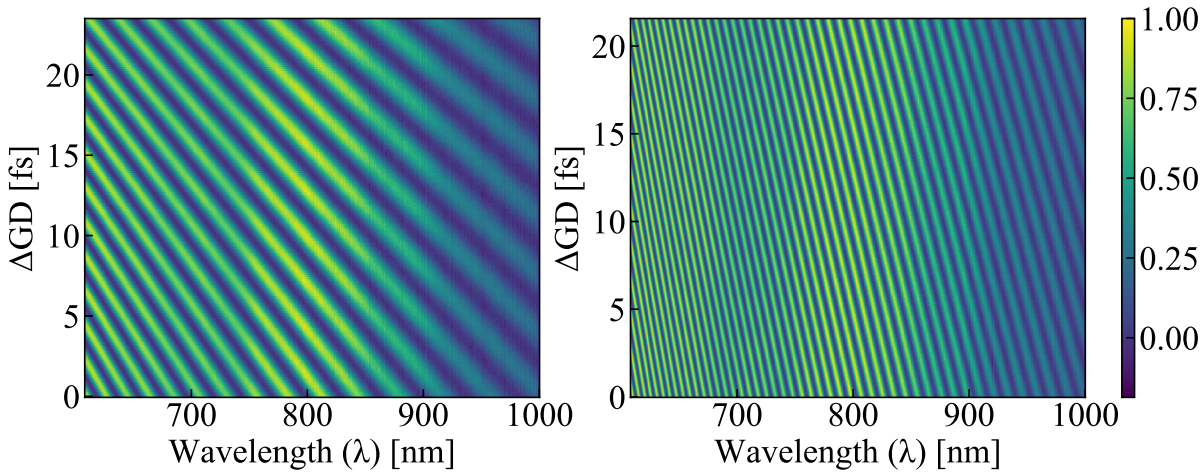

Figure 16: Quartz/fused silica (left). MgF_2/sapphire (right). Experimental spectrograms from both material combinations in the delay line. The spectral intensity is plotted over a 2D map of ΔGD and wavelength.

The FTSI methodology is employed and the RCC is extracted for both material combinations. This is plotted against the difference in group delay in Figure 17.

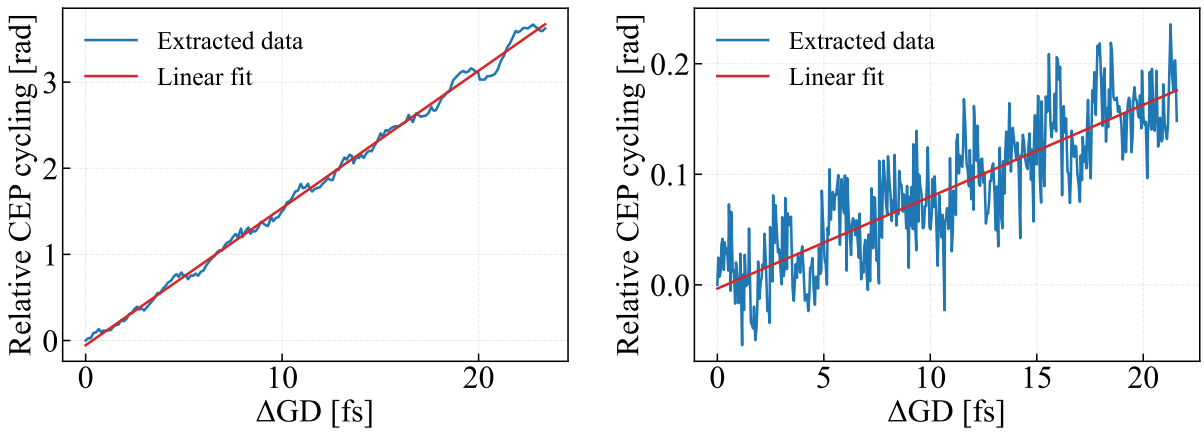

Figure 17: Quartz/fused silica (left). MgF_2/sapphire (right). The experimental relative CEP cycling data plotted over ΔGD. Using FTSI and a central wavelength of 750 nm. A linear function is fitted to the data. Over the evaluated relative group delay, the RCC for quartz/fused silica drifts by a significant 3 - 4 radians (approximately 0.5 cycles). In sharp contrast, the MgF_2/sapphire combination mitigates this drift, limiting the total RCC to below 0.2 radians (approximately 0.03 cycles).

The sawtooth artifacts observed in the simulations remain present in the experimental data. This confirms that these features stem from the discrete nature of the FTSI phase extraction algorithm, which is applied identically to both datasets.

Similar to the simulated analysis, the broadband behavior is evaluated by extracting the RCCR across the entire operational spectrum, rather than relying solely on the single-wavelength measurement at 750 nm. This broadband behavior is presented in Figure 18.

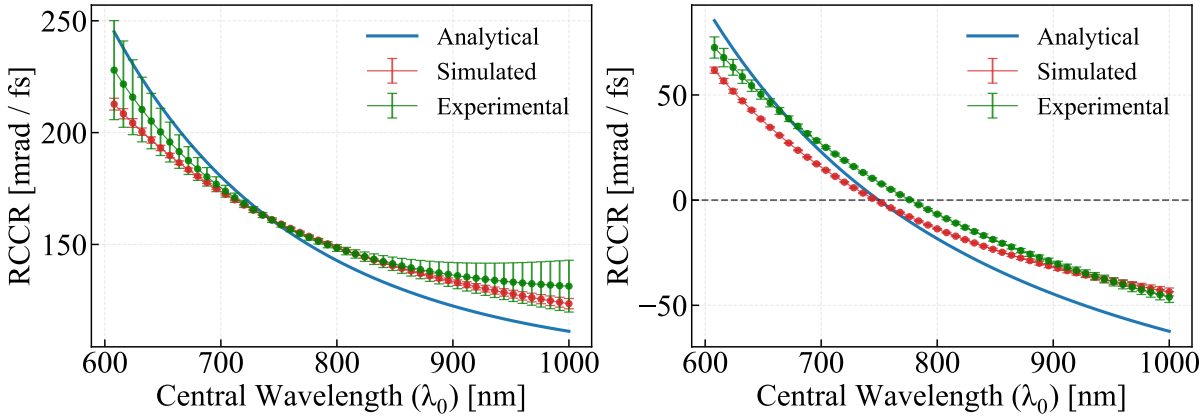

Figure 18: Left: the analytical, simulation and experimental RCCR curves plotted over central wavelength for the quartz/fused silica material combination used for the wedges in the birefringent delay line. No λ_{ZCR} can be identified for any of the curves. Right: RCCR curves plotted for MgF_2/sapphire. All curves cross a zero-cycling-rate. The experimental data exhibits a zero-cycling-rate at a λ_{ZCR} of 778.38 ± 0.78 nm.

As clearly demonstrated by the data in Figure 18, the quartz/fused silica setup fails to reach a zero-crossing at any point in the evaluated bandwidth. However, it is found that

the RCCR crosses horizontal axis in both theoretical models and in the experimental characterization of MgF_2/sapphire, confirming the existence of a central wavelength that results in a zero-cycling-rate within the measured spectral band. The λ_{ZCR} for the analytical curve is 749.59 nm, 747.11 ± 0.62 nm for the simulation, and 778.38 ± 0.78 nm for the experimental data.

Finally, to provide a direct comparison of the experimental data between the two material combinations, the relative CEP cycling rates of both are plotted together in Figure 19.

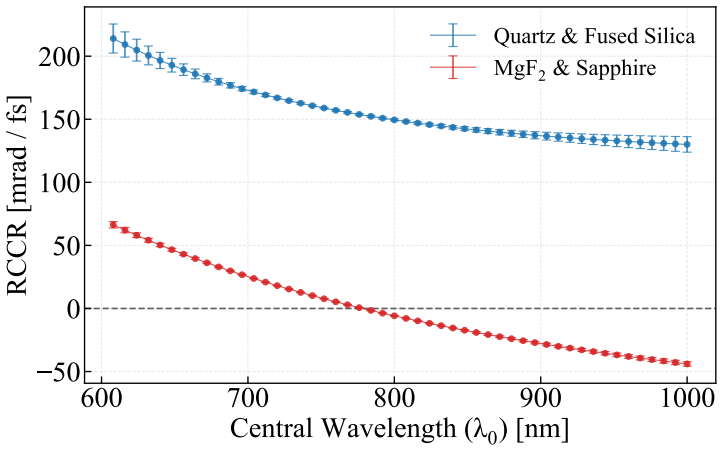

Figure 19: Relative CEP cycling rate for MgF_2/sapphire and quartz/fused silica material combinations plotted together over central wavelength. A clear difference is present. The RCCR in the range 725-825 nm is >10 times larger in the quartz/fused silica material combination compared to MgF_2/sapphire. Within the range 750-800 nm, the quartz/fused silica combination exhibits a >18 times larger RCCR.

The experimental characterization corroborates the theoretical and simulated models: the MgF_2/sapphire combination successfully demonstrates a zero-cycling-rate wavelength λ_{ZCR}, a feature entirely absent in the standard quartz-fused silica system. While there is a slight numerical deviation between the analytically predicted λ_{ZCR} and the experimentally observed value, this discrepancy is within the expected margins of errors. Ultimately, the fundamental proof of concept holds: a careful choice of birefringent materials can successfully eliminate relative CEP cycling at a specific central wavelength.

5 Discussion

It is clear that a distinct difference in the dispersive behavior is found when comparing the material combinations of the wedges. Most notably, the MgF_2/sapphire combination successfully demonstrates a zero-cycling-rate wavelength (λ_{ZCR}), a feature that is entirely absent in the standard quartz/fused silica system in the spectral range studied here.

However, it must be acknowledged that a numerical discrepancy exists between the analytically predicted, computationally simulated, and experimentally measured curves for the MgF_2/sapphire combination. While these deviations introduce uncertainty regarding the precise numerical value of λ_{ZCR}, they do not invalidate the underlying physical mechanism. The fundamental proof of concept: that pairing specific birefringent materials can eliminate relative CEP cycling, remains robustly supported across all three methods.

The experimental λ_{ZCR} (778.38 ± 0.78 nm) is 3.84% larger than the analytical value and 4.19 % larger than the simulated value. The observed discrepancies of between the theoretical and experimental results can be attributed to several theoretical and practical factors. Theoretically, as highlighted in subsubsection 3.1.1 (Figure 5), there is inherent ambiguity in the literature regarding the exact Sellmeier coefficients for these materials. For example, a re-analysis with the Sellmeier coefficients for MgF_2 with the data from Dodge [9] results in a λ_{ZCR} of 761.55 ± 0.58 nm and the data from H.H. Li [10] yield 766.56 ± 0.25 nm. This is in stark comparison to the obtained value using the coefficents from Zheng et al. [5], which give 747.11 ± 0.62 nm. This is a 2.60% increase for the H.H. Li coefficients and a 1.93% increase for the Dodge coefficients. Furthermore, this variance only accounts for the MgF_2 coefficients; incorporating literature variations for sapphire could reveal even larger theoretical discrepancies.

An additional source of experimental error arises from the method of application of the spectrometer's response function, which shows to have an impact on the final numerical values. To optimize this, fringe visibility and peak prominence are sought when applying the spectrometers response function. Future work could further minimize this error by systematically adjusting setup parameters and conducting a concurrent analysis of both the spectral and pseudo-time domains. It must nonetheless be emphasized that it is the proof-of-concept that is the core finding of the experimental characterization. Additionally, optical materials are rarely perfect; slight impurities, microscopic air inclusions, or minor deviations from a pristine crystalline structure in the laboratory wedges can alter their true dispersive properties. Given the ambiguities in the literature models, the empirically measured values, provided the optical and computational methodologies are robust, serve as the most accurate representation of the actual relative CEP cycling dynamics within these specific physical wedges.

The numerical discrepancy between the simulated and analytical λ_{ZCR} (0.33%) is exceptionally small, indicating that the FTSI method is extracting the phase from the spectral interferograms with high precision. However, a closer inspection of the curves in Figure 14 reveals that this deviation grows larger at the spectral tails. This can be primarily attributed to the windowing and isolation the positive peak during the FTSI process. The isolation and windowing inherently leaves some information of the phase in the peak out, leaving the result with a small discrepancy.

The precision of both the simulated and experimental data could be enhanced by refining

the Fourier Transform Spectral Interferometry (FTSI) extraction process. Specifically, the algorithm's windowing function must be addressed. Future data processing could mitigate the sawtooth artifact and loss of phase information by implementing more sophisticated signal processing techniques and greater spectral interpolation. Additionally, an implementation of statically locking the window position over the primary pulse could work if an artificially larger delay difference is introduced to minimize peak-overlapping in the pseudo-time domain.

6 Conclusion and Outlook

Standard quartz/fused silica setups introduce sub-optimal relative CEP cycling, but mathematically, computationally, and experimentally it has been shown here that pairing MgF_2 and sapphire in a birefringent delay line minimizes this and a stable λ_{ZCR} can be identified. Future researchers must account for the substantial variances in published Sellmeier coefficients when simulating novel material combinations. Due to these theoretical ambiguities, precise determination of a specific λ_{ZCR} strictly requires experimental validation.

Future researchers could reproduce this experiment to more precisely determine the exact wavelength for which a ZCR is achieved. Furthermore, an investigation into broadband optimization could yield interesting results. Further research could investigate this by finding a material with a RCCR as a function of central wavelength that has a flatter derivative and thus can have a wider range of minimized RCCR. This is relevant because a flatter derivative means the RCCR stays stable across a much wider spectral bandwidth, which could be applied to laser sources where the central wavelength can be tuned. A flatter derivative would also mean that the delay line could be used to address very different setups such as Ti:Sapphire based systems and Yb-based lasers. In that case, a flat derivative which minimizes the RCCR at both wavelengths would be favorable.

Finally, a database of λ_{ZCR} values for various material combinations could be compiled, enabling future researchers to tailor birefringent delay lines to specific laser spectra. However, as described in subsection 2.3, the fundamental relationship studied here relies on maintaining a strict 1-to-1 material substitution ratio between the wedges. Determining the optimal configuration for different insertion ratios would be highly beneficial, as it would eliminate the strict reliance on naturally occurring material properties. In theory, a variable substitution relationship would allow any pair of birefringent materials to achieve zero relative CEP cycling at any central wavelength, presenting a highly compelling avenue for future research.

References

[1] Nobel Prize Outreach AB. The nobel prize in physics 2023, 2023. https://www.nobelprize.org/prizes/physics/2023/summary/. Accessed: 2026-05-10.

[2] D. Brida, C. Manzoni, and G. Cerullo. Phase-locked pulses for two-dimensional spectroscopy by a birefringent delay line. *Optics Letters*, 37(15):3027–3029, 2012.

[3] L. Lepetit, G. Chériaux, and M. Joffre. Linear techniques of phase measurement by femtosecond spectral interferometry for applications in spectroscopy. *J. Opt. Soc. Am. B*, 12(12):2467–2474, 1995. Available at: https://opg.optica.org/josab/abstract.cfm?URI=josab-12-12-2467.

[4] Bahaa E. A. Saleh and Malvin Carl Teich. *Fundamentals of Photonics*. Wiley Series in Pure and Applied Optics. Wiley, Hoboken, NJ, third edition, 2019.

[5] Qifan Zheng, Xinchao Wang, and Dakotah Thompson. Temperature-dependent optical properties of monocrystalline CaF_2, BaF_2, and MgF_2. *Opt. Mater. Express*, 13(8):2380–2391, 2023. Available at: https://opg.optica.org/ome/abstract.cfm?URI=ome-13-8-2380.

[6] M. J. Dodge. Refractive index. In M. J. Weber, editor, *Handbook of Laser Science and Technology, Volume IV, Optical Materials: Part 2*, pages 30–43. CRC Press, Boca Raton, FL, 1986.

[7] Gorachand Ghosh. Dispersion-equation coefficients for the refractive index and birefringence of calcite and quartz crystals. *Optics Communications*, 163(1–3):95–102, 1999.

[8] I. H. Malitson. Interspecimen comparison of the refractive index of fused silica. *J. Opt. Soc. Am.*, 55(10):1205–1209, 1965. Available at: https://opg.optica.org/abstract.cfm?URI=josa-55-10-1205.

[9] Marilyn J. Dodge. Refractive properties of magnesium fluoride. *Appl. Opt.*, 23(12):1980–1985, 1984. Available at: https://opg.optica.org/ao/abstract.cfm?URI=ao-23-12-1980.

[10] H. H. Li. Refractive index of alkaline earth halides and its wavelength and temperature derivatives. *Journal of Physical and Chemical Reference Data*, 9(1):161–290, 1980. Available at: https://doi.org/10.1063/1.555616.

[11] Julius O. Smith. Hann (hanning) window, 2011. In: *Spectral Audio Signal Processing*. https://ccrma.stanford.edu/~jos/sasp/Hann_Hanning_Raised_Cosine.html. Accessed: 2026-04-27.

[12] Richard Baraniuk et al. Gibbs phenomena, 2020. In: *Signals and Systems*, Engineering LibreTexts. https://eng.libretexts.org/Bookshelves/Electrical_Engineering/Signal_Processing_and_Modeling/Signals_and_Systems_(Baraniuk_et_al.)/06%3A_Continuous_Time_Fourier_Series_(CTFS)/6.07%3A_Gibbs_Phenomena. Accessed: 2026-05-05.

[13] Simone Agha and Daniel Minkin. Understanding "walking the beam". Technical report, Stony Brook Laser Teaching Center, 2007. https://experimentationlab.berkeley.edu/sites/default/files/Mini-Project%20Report.pdf. Accessed: 2026-04-27.

Appendix A: Code

The code block below shows the FTSI loop that inputs interferograms, finds and isolates the positive peak in the time domain, and extracts the phase argument.

```
omega_cropped = (2 * np.pi * c) / (wavelengths * 1e-9)
omega_ascending = np.flip(omega_cropped)
spectrum_exp_asc = np.flip(spectrum_exp, axis=1)

w_min_exp, w_max_exp = np.min(omega_ascending), np.max(omega_ascending)
dw_exp = (w_max_exp - w_min_exp) / (len(omega_ascending) - 1)
N_padded_exp = (int(w_max_exp / dw_exp) + 1)*1
w_uniform_padded_exp = np.linspace(0, (N_padded_exp - 1) * dw_exp,
    N_padded_exp)

poly_coeffs_exp = []

sg_window = create_super_gaussian(omega_ascending, order=6, width_scale
    =0.95)

for i in range(len(d)):

    clean_spectrum = spectrum_exp_asc[i] * sg_window

    # Interpolate the cleaned spectrum onto the zero-padded axis
    interpolator = interp1d(omega_ascending, clean_spectrum, kind='cubic
    ', bounds_error=False, fill_value=0.0)
    spectrum_padded = interpolator(w_uniform_padded_exp)

    time_domain = np.fft.ifftshift(np.fft.ifft(spectrum_padded))
    time_axis = np.fft.ifftshift(np.fft.fftfreq(N_padded_exp, d=(dw_exp
    / (2 * np.pi))))

    peaks_indices, _ = find_peaks(np.abs(time_domain), prominence=np.max
    (time_domain)*0.2)

    # Filter for peaks that occur at positive time delays (e.g., after
    20 fs)
    valid_peaks = [i for i in peaks_indices if time_axis[i] > 20e-15]

    # Grab the most prominent peak in that valid window
    best_peak_idx = max(valid_peaks, key=lambda i: np.abs(time_domain)[i
    ])
    mypeak = time_axis[best_peak_idx]

    middle = mypeak * 1e15
    desired_width = 17 if k_val == 1 else 20
    t_start, t_end = (middle - desired_width) * 1e-15, (middle +
    desired_width) * 1e-15
```

```
    mask = (time_axis >= t_start) & (time_axis <= t_end)

    #Filter the positive peak
    time_domain_windowed = np.zeros_like(time_domain, dtype=complex)
    time_domain_windowed[mask] = time_domain[mask] * np.hanning(np.sum(mask))

    #Go back to spectral domain
    spec_domain = np.fft.fft(np.fft.fftshift(time_domain_windowed))

    #Extract phase
    unwrapped_phase = np.unwrap(np.angle(spec_domain))
    signal_mask = (w_uniform_padded_exp >= w_min_exp) & (w_uniform_padded_exp <= w_max_exp)
    w_fit = w_uniform_padded_exp[signal_mask]
    phase_fit = unwrapped_phase[signal_mask]
    poly_coeffs_exp.append(np.polyfit(w_fit, phase_fit, 3))
```

The code block below shows the code used to find the relative CEP cycling rate across a range of central wavelengths.

```
#Wavelength Sweep for CEP Cycling Rate vs central wavelength

lambdas_eval = np.linspace(608, 1000, 50)

def extract_rates(poly_coeffs_list, translation_array, lambdas_nm):
    rates, errors = [], []
    for l_nm in lambdas_nm:
        w0_curr = 2 * np.pi * c / (l_nm * 1e-9)
        a_phase, a_delay = [], []

        #Gather phase coeff.
        for p_coeffs in poly_coeffs_list:
            a_phase.append(np.polyval(p_coeffs, w0_curr))
            a_delay.append(w0_curr * np.polyval(np.polyder(p_coeffs), w0_curr))

        #Find slopes
        (aphase_slope, _), V_phase = np.polyfit(translation_array, np.unwrap(a_phase), 1, cov=True)
        (ad_slope, _), V_delay = np.polyfit(translation_array, np.array(a_delay), 1, cov=True)

        err_phase, err_delay = np.sqrt(V_phase[0, 0]), np.sqrt(V_delay[0, 0])
        time_d_slope_fs = (ad_slope / w0_curr) * 1e15

        #Calculate rate
        val_mrad_fs = (-k_val * (aphase_slope - ad_slope) /
```

```
    time_d_slope_fs) * 1000
25          rates.append(val_mrad_fs)
26
27          prefactor = abs(k_val * w0_curr * 1e-12)
28          err = prefactor * np.sqrt((err_phase / ad_slope)**2 + (
    aphase_slope * err_delay / ad_slope**2)**2)
29          errors.append(err)
30      return np.array(rates), np.array(errors)
31
32 rates_sim, errs_sim = extract_rates(poly_coeffs_sim, d, lambdas_eval)
33 rates_exp, errs_exp = extract_rates(poly_coeffs_exp, d, lambdas_eval)
```